Micro-pulse polarization lidar at 1.5 μm using a single superconducting nanowire single-photon detector

Jiawei Qiu, Haiyun Xia,* Mingjia Shangguan, Xiankang Dou, Manyi Li, Chong Wang, Xiang Shang, Shengfu Lin, and Jianjiang Liu

CAS Key Laboratory of Geospace Environment, University of Science and Technology of China, Hefei, 230026, China
*Corresponding author: hsia@ustc.edu.cn

An all-fiber, eye-safe and micro-pulse polarization lidar is demonstrated with a polarization-maintaining structure, incorporating a single superconducting nanowire single-photon detector (SNSPD) at 1.5 μm. The time-division multiplexing technique is used to achieve a calibration-free optical layout. A single piece of detector is used to detect the backscatter signals at two orthogonal states in an alternative sequence. Thus, regular calibration of the two detectors in traditional polarization lidars is avoided. The signal-to-noise ratio of the lidar is guaranteed by using an SNSPD, providing high detection efficiency and low dark count noise. The linear depolarization ratio (LDR) of the urban aerosol is observed horizontally over 48 h in Hefei [N31°50′37″, E117°15′54″], when a heavy air pollution is spreading from the north to the central east of China. Phenomena of LDR bursts are detected at a location where a building is under construction. The lidar results show good agreement with the data detected from a sun photometer, a 532 nm visibility lidar, and the weather forecast information.   © 2017 Optical Society of America

Aerosols have heterogeneous effects on the health of residents [1,2]. Moreover, studies show that the formation of clouds and cyclones is modulated by the aerosols [3]. Lidar can make continuous aerosol detection with both high spatial and temporal resolutions [4–8]. Particularly, since its first demonstration in 1971, the polarization lidar has shown the capability of identifying different types of aerosols and clouds by analyzing the linear depolarization ratio (LDR) [9–15].

In order to improve the performance of the polarization lidar, extensive efforts have been done. For example, in 1982, an airborne polarization lidar is demonstrated for the mea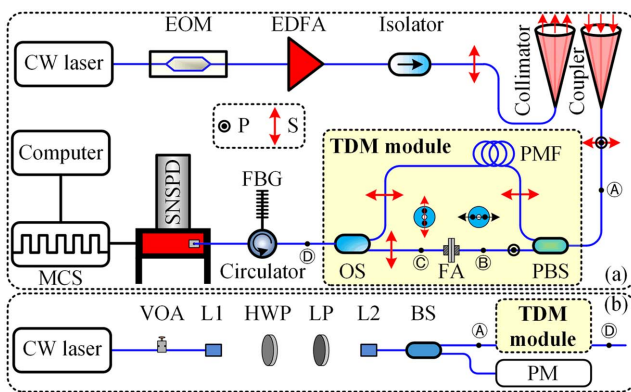surement of the LDR of the ice and water clouds with a 532 nm pulsed laser in the 19 km operation altitude [16]. Since 2006, the polarization lidar cloud-aerosol lidar with orthogonal polarization on board the satellite Cloud-Aerosol Lidar and Infrared Pathfinder Satellite Observations is able to provide vertical profiles and the LDR of aerosols and clouds from the orbit [17]. It applies high-pulse-energy (110 mJ) lasers at 532 nm (polarization sensitive) and 1064 nm, with a 1 m telescope. To measure the depolarization effect of urban aerosols, an eye-safe polarization lidar is demonstrated at 1.54 μm in 2007 [18], in which a high-pulse-energy (225 mJ) Raman-shifted laser and a 400 mm telescope are applied. The backscatter signals from the white smoke and the road dust are successfully distinguished via different LDR values. In order to eliminate the mismatch of the two detectors which are used to detect signals at two orthogonal polarization states in traditional lidars, optical receivers using a single detector are demonstrated in 2009, either by modulating the polarization state of the outgoing laser [19] or by inserting an optical switch (OS) into the receiver [20]. In such modifications, one can realize detection of the backscatter signals at two polarization states alternately. However, the orthogonal signals are not backscattered from the same aerosols in the detection volume, since aerosols vary fast both in space and in time. Furthermore, the power fluctuation of the outgoing laser will also introduce systematic error.

To resolve these challenges, an all-fiber eye-safe polarization lidar incorporating a time-division multiplexing (TDM) technique is demonstrated. Instead of using a large-aperture telescope and high-pulse-energy lasers, a superconducting nanowire single-photon detector (SNSPD) with the outstanding performance of high quantum efficiency, low dark count noise, and no afterpulsing is used to guarantee the high signal-to-noise ratio at 1.5 μm.

The schematic of the polarization lidar is shown in Fig. 1(a). The parallel and perpendicular polarization states of the light are labeled as P and S, respectively. In the transmitter system, a single longitudinal mode laser at 1548.1 nm is produced by a seed laser. The continuous-wave (CW) laser is chopped into a pulse train by using an electro-optic modulator (EOM), which is driven by an electric pulse generator (PG) with a pulse

repetition rate of 9.5 kHz. The pulse width of the laser is set to 200 ns, resulting in a spatial resolution of 30 m. Then the energy of a laser pulse is amplified to 100 μJ by using a polarization-maintaining erbium-doped fiber amplifier (EDFA). The polarization extinction ratio of the pulsed laser is 30.2 dB after the isolator, which will introduce a systematic error of 0.1% to the LDR measurement. The amplified pulsed laser is collimated and sent to the atmosphere via an 80 mm collimator, which delivers a divergence of 40.0 μrad. The backscatter signal from the atmosphere is collected and coupled into a single-mode polarization-maintaining fiber by using an 80 mm coupler, which has a field of view (FOV) of 47.6 μrad. Thanks to the narrow FOV adopted in this lidar, the background noise from the sky is suppressed.

In the receiver system, a TDM module is implemented to separate the two orthogonal backscatter signals in the time domain. The backscatter signals at two orthogonal polarization states are divided into two channels by using a polarization-maintaining polarization beam splitter (PBS). The polarization extinction ratio of the PBS is 30.4 dB for the two polarization channels. This will also introduce another systematic error at about 0.1%. The time sequence of the signal acquisition is shown in Fig. 2. Since the detection error is determined by the signal-to-noise ratios in both channels, the P component, which is stronger, is chosen to be delayed and attenuated in the polarization-maintaining fiber (PMF). Usually the intensity of the backscatter signal at the S state is about 10% of the value at the P state. The time delay of the backscatter signal at the S state is optimized according to its intensity and how far it can stretch. As shown in Fig. 1(a), the P component goes through the upper branch of the PBS. It propagates along an 8060 m PMF, resulting in a transmittance of 68.4%. Since the refractive index of the PMF is 1.5, a time delay of 40.3 μs is realized, resulting in a detection range of 6045 m. Then the signal is fed to the OS. The S component goes through the bottom branch of the PBS. At point B,

the polarization plane is aligned at the slow axis of the PMF. Then the signal goes through a fiber adaptor and reaches point C, with the polarization plane also aligned to the slow axis of the PMF at the right-down tap of the OS. The OS is driven by a PG synchronized to the input of the EOM. In such a way, the signals at two polarization states are selected and delivered by the OS alternately. It is worth mentioning that a fiber coupler can replace the OS, but it is not recommended. The reason is that the insertion loss of a fiber coupler is larger than 3 dB, which is much higher than that of the OS (0.8 dB). In addition, the fiber coupler leads to an overlap of the two orthogonal signals. In the contrast, the crosstalk between the two channels of the OS is –35 dB. The overlap of the signal from two polarization channels can be suppressed.

After the OS, a fiber Bragg grating with a narrow band of 8 pm is used in conjunction with a circulator, which provides a background noise suppression of 35 dB. Finally, the two orthogonal components are detected on the SNSPD (Single Quantum, Eos 210C) alternately. The SNSPD has a quantum efficiency of 60% and a dark count rate of 100 Hz. The superconducting nanowire inside the helium dewar is kept at a superconducting state at a temperature of 3.2 K, incorporating a helium refrigeration system. When a photon from the backscatter signal hits the nanowire, it will break the superconducting state and produce a voltage pulse. After recording the voltage pulse, the nanowire will recover to the superconducting state in 10 ns and be ready for the next photon detection. The SNSPD converts the photon events to electric pulses and delivers it to a multi-channel scaler. The bin width of the multi-channel scaler is set to 30 m, consistent with the pulse width of laser. After an accumulation of over one minute, the signal is sent to a computer for real-time data processing.

Compared to polarization lidars at other wavelengths, the 1.5 μm polarization lidar has some outstanding merits. It allows the detection of large particle aerosols, which is important for PM10 analysis in polluted atmosphere [21]. The daytime measurement is allowed, since the background signal from the sky at 1.5 μm is weaker than that at visible wavelengths. The micropulse laser enables an all-fiber structure of the polarization lidar, which tremendously shrinks the size of the system. In addition, thanks to commercial available components widely used in the optic telecommunications, a polarization lidar at 1.5 μm can be assembled economically. All devices in the system are polarization-maintaining devices, which guarantee the polarization stability of the system. Moreover, only in the communication band of 1.5 μm, the TDM method can be adopted,
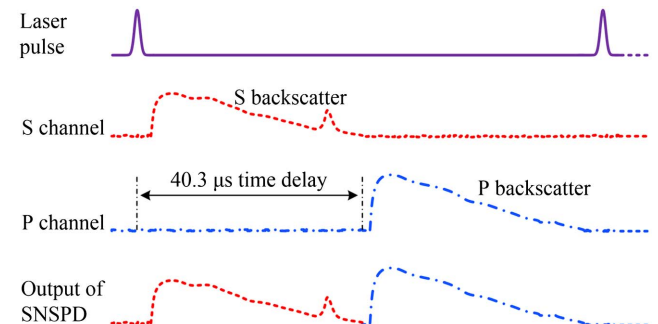
Fig. 1. (a) Optical layout of the polarization lidar. EOM, electro-optic modulator; PG, pulse generator; EDFA, erbium-doped fiber amplifier; PBS, polarization beam splitter; PMF, polarization-maintaining fiber; FA, fiber adaptor; OS, optical switch; FBG, fiber Bragg grating; SNSPD, superconducting nanowire single-photon detector; MCS, multi-channel scaler; P, parallel polarization; S, perpendicular polarization; (b) calibration layout. VOA, variable optical attenuator; L1, first lens as a collimator; L2, second lens as a coupler; HWP, half-wave plate; LP, linear polarizer; BS, polarization-maintaining beam splitter; PM, power meter.

Fig. 2. Timing sequence of data acquisition for a single pulse. S channel, perpendicular channel; P channel, parallel channel.

which allows simultaneous detection of the signals at two orthogonal polarization states with a single detector [22]. Thanks to the usage of the TDM module, the system saves the cost of a second SNSPD channel. This makes the system immune to the fluctuations on the laser power and detection efficiency, which means regular calibrations of the lidar are not necessary. Therefore, this novel polarization lidar is particularly suitable for long-term routine operation in harsh environments such as aboard aircraft or satellites.

The lidar equations of the polarization lidar at two polarization channels are expressed as Eqs. (1) and (2):

$$N_\parallel(R) = E_0 \frac{\eta_q}{h\nu} \frac{A_0}{R^2} \xi(R) \beta_\parallel k_\parallel \, \exp\left[-2\int_0^R \sigma_\parallel(r)\mathrm{d}r\right], \quad \textbf{(1)}$$

$$N_\perp(R) = E_0 \frac{\eta_q}{h\nu} \frac{A_0}{R^2} \xi(R) \beta_\perp k_\perp \, \exp\left\{-\int_0^R [\sigma_\parallel(r) + \sigma_\perp(r)]\mathrm{d}r\right\}, \quad \textbf{(2)}$$

where N is the photon counts detected in the two channels, E_0 is the energy of the laser pulse, η_q is the quantum efficiency of the detector, h is the Plank constant, ν is the frequency of the laser, A_0 is the area of the telescope, $\xi(R)$ is the geometrical overlap factor at range R, $\beta_\parallel$ and $\beta_\perp$ are the atmospheric backscatter coefficients at two orthogonal polarization states, σ is the extinction coefficient, and k is the attenuation coefficient in the TDM module. Approximately, $\sigma_\parallel = \sigma_\perp$. Thus, the LDR can be defined as [8]

$$\delta(R) = k_\parallel N_\perp(R)/k_\perp N_\parallel(R) = kN_\perp(R)/N_\parallel(R), \quad \textbf{(3)}$$

where the calibration coefficient k is mainly affected by the attenuation of the 8 km PMF and the insertion losses in the two channels of the TDM module. Since the coupler is fabricated with a single piece of convex lens, it has the same transmittance for the backscatter signals at two orthogonal polarization states.

The optical layout of calibration is shown in Fig. 1(b). The polarization controller consists of two lenses, a half-wave plate (HWP) and a linear polarizer (LP). The extinction ratio of the LP is 50 dB. This structure can convert the linear polarization state of the laser to either the P state or the S state. The laser source in the calibration system is a single longitude mode CW laser attenuated by using a polarization-maintaining variable optical attenuator (VOA). Using a 1:99 PBS, 99% of the laser power is guided to a low polarization dependence power meter (Keysight, 81634B) to monitor the laser power, which shows a relative uncertainty due to polarization of less than ±0.005 dB. Note that, in order to identify the signals in two polarization channels in the time domain, the OS in the TDM module and the MCS work synchronously. The calibration procedure goes as follows. First, rotate the LP to make the count rate in the P channel getting its maximum. In other words, the output of the LP is all sent to the P channel in the TDM. Secondly, rotate the HWP to get a maximum count rate in the P channel as $E_\parallel$ and, meanwhile, record the reading on the power meter as $P_\parallel$. Then turn to the S state and get the reading $E_\perp$ and $P_\perp$. Thus, the calibration factor k is calculated as

$$k = E_\parallel P_\perp / E_\perp P_\parallel. \quad \textbf{(4)}$$

After the calibration, the stability of the system is tested using an amplified spontaneous emission fiber source, which delivers lights at arbitrary polarization states after going through
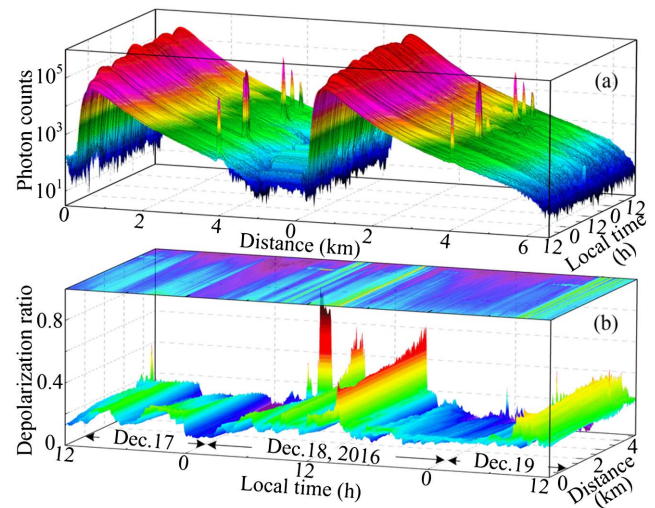

Fig. 3. (a) Raw signal of the polarization lidar over 48 h and (b) 48 h continuous measurement results of the LDR.

an integrating sphere [22]. A measurement error less than 0.23% is realized over 10 days.

A continuous observation of the LDR was carried out on the campus of the University of Science and Technology of China (N31°50′37″, E117°15′54″). The experiment starts at 12:00 on December 17, 2016 and ended at 12:00 on December 19, 2016. The laser beam points to north horizontally on the top of a research building. A 532 nm visibility lidar, a sun photometer, and a wind sensor are also applied for references.

The raw signal detected by the polarization lidar is shown in Fig. 3(a). The calculated LDR is shown in Fig. 3(b). One can find that there were two bursts of the LDR at 15:00, December 18, 2016 and 10:00, December 19, 2016. The wind sensor shows that the north wind strengthens, but changes to south wind soon at these moments. The emissions of thermal power plants and factories in the northern industry area are brought to the south of the city. In Fig. 3(a), one can find several spikes on the surface of the backscatter signals.
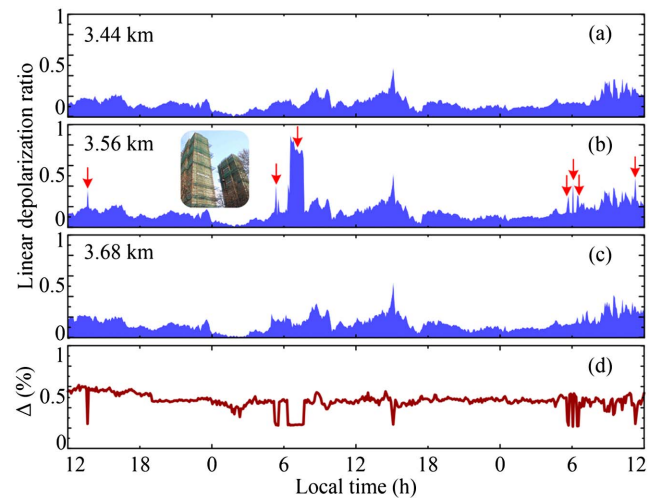
Fig. 4. LDR at the location of (a) 3.44, (b) 3.56, and (c) 3.68 km away from the lidar; the red arrows indicate the moments of the bursts of the LDR. (d) Measurement error of the LDR at 3.56 km. The inset is a photo of the building under construction.
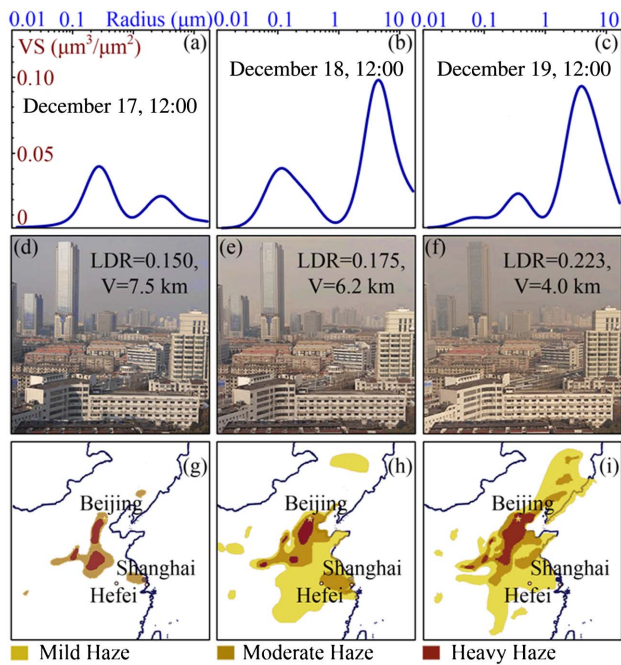
Fig. 5. (a)–(c) Volume spectrum detected by a sun photometer in the experiment; (d)–(f) visibility data and photographs of the scene in the experiment; (g)–(i) haze distribution forecast released by the China Meteorological Administration in the experiment. VS, volume spectrum; V, visibility.

Besides, Fig. 3(b) also shows that the spikes in Fig. 3(a) are consistent with sudden increases of the LDR. The LDRs at the distance of 3.44, 3.56, and 3.68 km are plotted in Fig. 4, for comparison. The bursts of LDRs are tagged with red arrows in Fig. 4(b). However, in the range bins 120 m before and behind 3.56 km, no spikes are found, as shown in Figs. 4(a) and 4(c). It turns out that a building is under construction at the point, shown as the inset in Fig. 4(b). Considering that these events appear in the daytime only, the phenomena are most likely due to the construction dusts. Since the aerosol number density of the construction dusts is quite high, the large LDR values may be due to the multiple scattering effects. The data shown in Fig. 4(d) are the measurement error of the LDR, which is a sum of the statistical standard error and the systematic errors caused by the polarization extinction ratio of the laser and the PBS. The statistical standard error is dominated by the photon counting fluctuation, which is supposed to follow a Poisson distribution [23,24].

The sun photometer (Cimel, CE-318) is installed on the top of the building in the experiment. It can detect the volume spectrum of aerosols with the diameter ranging from 12.09 nm to 16.5 µm. The typical bimodal distributions of the volume spectrum in the three days are shown in Figs. 5(a)–5(c). An increase of aerosol particles with a large diameter from December 17 to December 18 is found. Such an air condition continued to the next day. This is coincident with the increase of LDR detected by the polarization lidar at the corresponding moments.

The visibility lidar working at 532 nm are used to detect the atmospheric visibility in the experiment. The visibility data are shown in Figs. 5(d)–5(f), with the photographs of the scene. From December 17 to December 19, as the visibility gets worse, the averaged LDR rises at noon. This phenomenon has also been reported [25].

The haze distributions over the three days are released by the China Meteorological Administration, as shown in Figs. 5(g)–5(i). From December 17 to December 19, 2016, central eastern China was suffering from heavy hazy weathers. Then the haze was brought to Hefei and Shanghai by the north winds. The hazy atmosphere in Hefei is recorded by the polarization lidar. As shown in Fig. 3(b), the LDR on December 17 is lower than 0.2. However, when the haze arrived at Hefei on December 18, peak LDRs over 0.5 and 0.4 were detected on December 18 and 19, respectively.

A 1.5 µm micro-pulse polarization lidar incorporating single-channel SNSPD is demonstrated. A continuous observation of atmospheric LDR over 48 h is taken. The lidar records the evolution process of aerosol in Hefei from December 17, 2016 to December 19, 2016. With 1 min temporal resolution and 30 m spatial resolution, a detection range of 4 km is reached horizontally. The detection results are in good agreement with the observation results of the sun photometer and the visibility lidar.

REFERENCES

1. Q. Zhang, K. He, and H. Huo, Nature **484**, 161 (2012).
2. Z. Zhang, J. Wang, L. Chen, X. Chen, G. Sun, N. Zhong, H. Kan, and W. Lu, Environ. Sci. Pollut. Res. **21**, 4236 (2014).
3. Y. Wang, R. Zhang, and R. Saravanan, Nat. Commun. **5**, 3098 (2014).
4. H. Xia, G. Shentu, M. Shangguan, X. Xia, X. Jia, C. Wang, J. Zhang, J. S. Pelc, M. M. Fejer, Q. Zhang, X. Dou, and J. Pan, Opt. Lett. **40**, 1579 (2015).
5. C. Xie, T. Nishizawa, N. Sugimoto, I. Matsui, and Z. Wang, Appl. Opt. **47**, 4945 (2008).
6. H. Xia, M. Shangguan, C. Wang, G. Shentu, J. Qiu, Q. Zhang, X. Dou, and J. Pan, Opt. Lett. **41**, 5218 (2016).
7. M. Shangguan, H. Xia, C. Wang, J. Qiu, G. Shentu, Q. Zhang, X. Dou, and J. Pan, Opt. Express **24**, 19322 (2016).
8. M. Shangguan, H. Xia, C. Wang, J. Qiu, S. Lin, X. Dou, Q. Zhang, and J. Pan, Opt. Lett. **42**, 3541 (2017).
9. K. Sassen, Am. Meteorol. Soc. **72**, 1848 (1991).
10. S. Groß, M. Esselborn, B. Weinzierl, M. Wirth, A. Fix, and A. Petzold, Atmos. Chem. Phys. **13**, 2487 (2013).
11. A. Konoshonkin, Z. Wang, A. Borovoi, N. Kustova, D. Liu, and C. Xie, Opt. Express **24**, A1257 (2016).
12. B. Liu and Z. Wang, Opt. Express **21**, 14583 (2013).
13. H. Di, D. Hua, L. Yan, X. Hou, and X. Wei, Appl. Opt. **54**, 389 (2015).
14. C. Wu and F. Yi, J. Geophys. Res. **122**, 4479 (2017).
15. W. Kong and F. Yi, J. Geophys. Res. **120**, 7928 (2015).
16. J. Spinhirne, M. Hansen, and L. Caudill, Appl. Opt. **21**, 1564 (1982).
17. D. Winker, M. Vaughan, A. Omar, Y. Hu, and K. Powell, J. Atmos. Ocean. Tech. **26**, 2310 (2009).
18. S. Mayor, S. Spuler, B. Morley, and E. Loew, Opt. Eng. **46**, 096201 (2007).
19. C. Flynn, A. Mendoza, Y. Zheng, and S. Mathur, Opt. Express **15**, 2785 (2007).
20. P. Dubey, S. Jain, B. Arya, and P. Kulkarni, Rev. Sci. Instrum. **80**, 053111 (2009).
21. S. Lisenko, M. Kugeiko, and V. Khomich, Atmos. Ocean. Opt. **29**, 288 (2016).
22. C. Wang, H. Xia, M. Shangguan, Y. Wu, L. Wang, L. Zhao, J. Qiu, and R. Zhang, Opt. Express **25**, 20663 (2017).
23. H. Xia, D. Sun, Y. Yang, F. Shen, J. Dong, and T. Kobayashi, Appl. Opt. **46**, 7120 (2007).
24. H. Xia, X. Dou, D. Sun, Z. Shu, X. Xue, Y. Han, D. Hu, Y. Han, and T. Cheng, Opt. Express **20**, 15286 (2012).
25. D. Bäumer, B. Vogel, S. Versick, R. Rinke, O. Möhler, and M. Schnaiter, Atmos. Environ. **42**, 989 (2008).